

Defect Engineering in Plasmonic Metal Oxide Nanocrystals

Evan L. Runnerstrom,^{†,‡} Amy Bergerud,^{†,‡,§} Ankit Agrawal,[‡] Robert W. Johns,^{‡,||} Clayton J. Dahlman,[‡] Ajay Singh,[‡] Sverre M. Selbach,[§] and Delia J. Milliron^{*,‡}

[†]Department of Materials Science and Engineering, The University of California, Berkeley, Berkeley, California 94720, United States

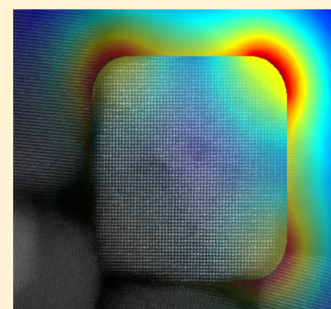
[‡]McKetta Department of Chemical Engineering, The University of Texas at Austin, Austin, Texas 78712-1589, United States

[§]Department of Materials Science and Engineering, Norwegian University of Science and Technology, 7491 Trondheim, Norway

^{||}Department of Chemistry, The University of California, Berkeley, Berkeley, California 94720, United States

S Supporting Information

ABSTRACT: Defects may tend to make crystals interesting but they do not always improve performance. In doped metal oxide nanocrystals with localized surface plasmon resonance (LSPR), aliovalent dopants and oxygen vacancies act as centers for ionized impurity scattering of electrons. Such electronic damping leads to lossy, broadband LSPR with low quality factors, limiting applications that require near-field concentration of light. However, the appropriate dopant can mitigate ionized impurity scattering. Herein, we report the synthesis and characterization of a novel doped metal oxide nanocrystal material, cerium-doped indium oxide (Ce:In₂O₃). Ce:In₂O₃ nanocrystals display tunable mid-infrared LSPR with exceptionally narrow line widths and the highest quality factors observed for nanocrystals in this spectral region. Drude model fits to the spectra indicate that a drastic reduction in ionized impurity scattering is responsible for the enhanced quality factors, and high electronic mobilities reaching 33 cm²V⁻¹s⁻¹ are measured optically, well above the optical mobility for tin-doped indium oxide (ITO) nanocrystals. We investigate the microscopic mechanisms underlying this enhanced mobility with density functional theory calculations, which suggest that scattering is reduced because cerium orbitals do not hybridize with the In orbitals that dominate the bottom of the conduction band. Ce doping may also reduce the equilibrium oxygen vacancy concentration, further enhancing mobility. From the absorption spectra of single Ce:In₂O₃ nanocrystals, we determine the dielectric function and by simulation predict strong near-field enhancement of mid-IR light, especially around the vertices of our synthesized nanocubes.



KEYWORDS: Nanocrystal, doping, plasmonics, near-field enhancement, density functional theory, cerium-doped indium oxide

Doped metal oxide nanocrystals display intriguing composition-dependent properties. Chief among these is near- to mid-infrared (NIR/MIR) localized surface plasmon resonance (LSPR), which is induced by n-type doping to generate free electrons that can participate in light-driven free carrier oscillation at tunable resonant frequencies. Colloidal synthesis has enabled the discovery of several doped metal oxide nanocrystals with LSPR over the past decade. Key examples include aluminum-doped zinc oxide (AZO),¹ indium-doped cadmium oxide (ICO),² and tin-doped indium oxide (ITO or Sn:In₂O₃).³ These materials have been studied as thin films for their transparent conductive properties, and the dielectric functions known from such studies are the basis for understanding the LSPR properties of the corresponding nanocrystals.

LSPR excitations are confined to the physical dimensions of nanocrystals and effectively concentrate light into volumes well below the diffraction limit. As a result, very intense local field “hotspots” are formed around the nanocrystals that can interact with nearby molecules or materials. This near-field enhancement makes doped metal oxide nanocrystals good candidates for NIR and MIR near-field optics and enhanced spectroscopies like surface-enhanced infrared absorption spectroscopy

(SEIRA). Efficient hot spot generation requires a high quality factor (Q , the ratio of the peak energy to the width of the LSPR peak), which implies longer plasmon lifetimes, weaker electronic damping, and stronger near-field intensities. Thus, it is important to consider not only how dopants in metal oxides tune the LSPR frequency by changing the free carrier concentration but also how their presence contributes to damping by scattering the oscillating free electrons. To create high- Q MIR plasmonic materials, strategies are needed to minimize scattering even as substantial concentrations of dopants are introduced.

To account for both free carrier concentration and electronic damping, the dielectric function of a doped oxide nanocrystal can be represented by the Drude model extended to include a frequency-dependent contribution to the damping of oscillating free carriers

Received: March 18, 2016

Revised: April 18, 2016

Published: April 25, 2016

$$\varepsilon(\omega) = \varepsilon_{\infty} - \frac{\omega_p^2}{\omega^2 + i\omega\Gamma(\omega)} \quad (1)$$

where ε_{∞} is the high-frequency permittivity, $\Gamma(\omega)$ is the electronic damping function, and ω_p is the plasma frequency, proportional to the square root of the carrier concentration. The magnitude of Γ is critical because it determines the LSPR line width (i.e., Q) and its functional form reflects the frequency dependence of electronic scattering by charged point defects; such ionized impurity scattering acutely hampers electron transport and reduces mobility. This is particularly important for doped metal oxides, as aliovalent dopants are necessary for free carrier generation, and oxygen vacancies, as doubly ionized defects, scatter electrons four times more strongly than singly ionized defects.^{4–6} LSPR behavior therefore depends critically on how dopants influence defect chemistry, carrier scattering, and mobility. We recently demonstrated the importance of defects in determining LSPR properties by showing that Sn:In₂O₃ nanocrystals with surface-segregated tin display significantly narrower and more symmetric LSPR peaks compared to nanocrystals with homogeneously distributed tin owing to a decrease in ionized impurity scattering.⁷

Deliberate defect engineering, that is, rational dopant selection and minimization of vacancy concentration, has been explored in transparent conducting oxide thin films as a viable strategy to combat ionized impurity scattering. For example, Mo-doped In₂O₃ thin films have higher electron mobility than Sn:In₂O₃. Unlike Sn orbitals, Mo orbitals do not hybridize with the conduction band minimum (CBM), leading to stronger electrostatic screening of dopant potentials and reduced ionized impurity scattering.⁸ Likewise, Dy-doped CdO thin films exhibit exceptional electronic mobility and large predicted plasmon quality factors because Dy dopants modify the defect equilibria to minimize oxygen vacancy concentration.⁹ Doping with Dy³⁺ also minimizes local strain and the associated electron–phonon scattering because it is a close match to Cd²⁺ in ionic radius.

Applying these strategies to indium oxide reveals cerium as a promising dopant. Cerium is significantly more electropositive than In and Sn, which implies that Ce states may lie within the conduction band of In₂O₃, limiting hybridization at the CBM and leading to remote screening of dopants as in Mo-doped In₂O₃. As an electropositive dopant, Ce may also be a more energetically stable electron donor than oxygen vacancies, which could modify the defect equilibria to inhibit oxygen vacancy formation. Finally, the six-coordinate crystal ionic radius of Ce⁴⁺ (101 pm) is a closer match to In³⁺ (94 pm) than is Sn⁴⁺ (83 pm),¹⁰ which implies that cerium doping may reduce lattice strain compared to Sn:In₂O₃ in a manner analogous to Dy in CdO. We therefore hypothesized that cerium-doped indium oxide (Ce:In₂O₃) nanocrystals would display higher electronic mobility and higher Q LSPR peaks compared to Sn:In₂O₃. The few literature accounts of Ce-doped In₂O₃ thin films report high mobility, which supports this hypothesis, though these studies used tin or hydrogen as codopants and did not study the microscopic mechanisms responsible for enhanced mobility.^{11,12}

For the first time, we synthesized colloidal Ce:In₂O₃ nanocrystals by adapting a typical procedure used to synthesize Sn:In₂O₃ nanocrystals.^{8,7} In brief, indium acetylacetonate, a cerium precursor, and oleylamine were mixed and heated to 250 °C for 2 h to form colloidal nanocrystals under an inert atmosphere using standard Schlenk line techniques. Doping

levels were measured with inductively coupled plasma optical emission spectroscopy (ICP-OES). Transmission electron microscopy (TEM, Figure 1a–d and Figure S1) reveals that

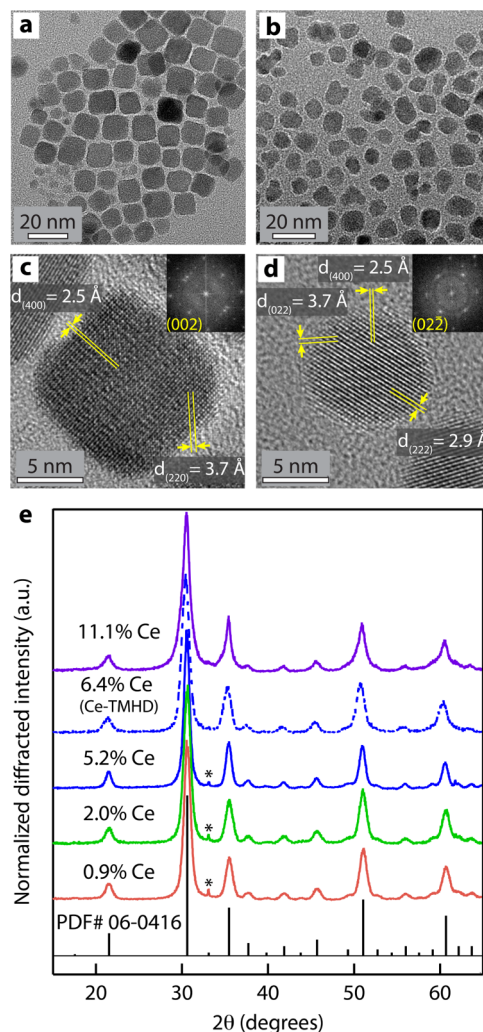


Figure 1. Physical characterization of Ce:In₂O₃ nanocrystals. (a) TEM micrograph of cubic Ce:In₂O₃ nanocrystals doped with 5.2% Ce (from Ce-acac). (b) TEM micrograph of pseudospherical Ce:In₂O₃ nanocrystals doped with 6.4% Ce (from Ce-TMHD). (c) HRTEM image of cubic nanocrystal with FFT in inset. (d) HRTEM of spherical nanocrystal with FFT in inset. (e) Representative powder XRD patterns for Ce:In₂O₃ nanocrystals, confirming the indium oxide cubic bixbyite structure (reference PDF pattern shown at bottom). The sharp peaks marked with a (*) are due to the substrate.

the nanocrystals are relatively uniform and highly crystalline. X-ray diffraction (XRD, Figure 1e) confirms the crystallinity of Ce:In₂O₃ nanocrystals, which have the cubic bixbyite crystal structure typical of bulk In₂O₃, without detectable impurity phases. Rietveld refinement performed on the XRD patterns (Figure S2) showed that the lattice parameter increased slightly with Ce doping along a trajectory well-fit by Vegard's law. Owing to the larger ionic radius of cerium, this lattice expansion signifies effective substitutional dopant incorporation. We prepared a doping series from 0% Ce to 11.1% Ce using cerium acetylacetonate (Ce-acac) as a dopant source, and we also evaluated other precursors, namely cerium tetramethylheptanedionate (Ce-TMHD), cerium ammonium nitrate, and cerium acetate. All dopant precursors produced colloiddally

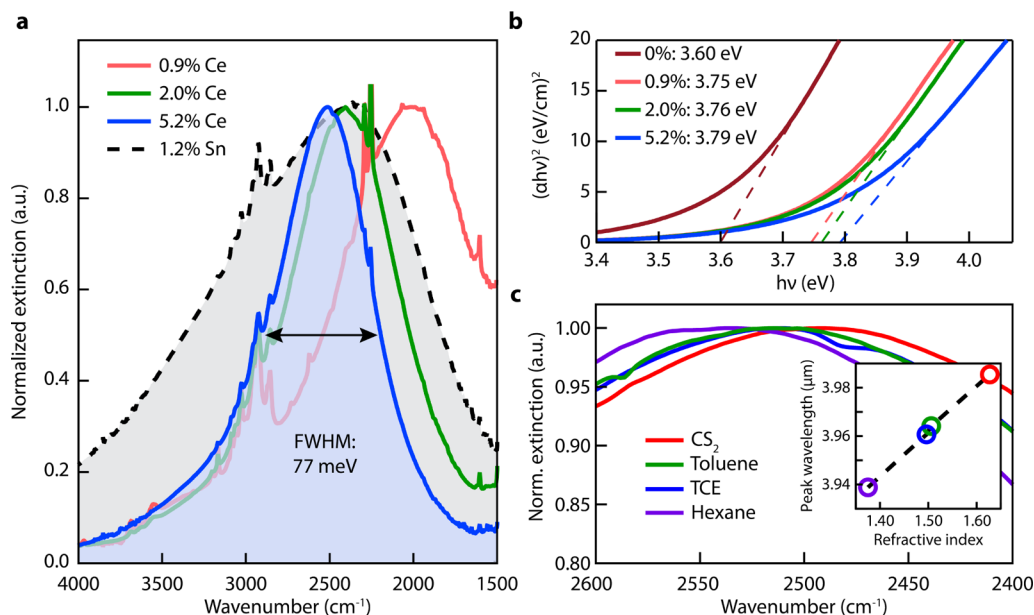


Figure 2. Optical properties of Ce:In₂O₃ nanocrystals. (a) FTIR liquid cell spectra of Ce:In₂O₃ and Sn:In₂O₃ nanocrystals dispersed in tetrachloroethylene showing narrow and tunable MIR LSPR of Ce:In₂O₃. (b) Tauc plot showing systematic increase of Ce:In₂O₃ optical bandgap with Ce content consistent with a Burstein–Moss shift. (c) LSPR of 5.2% Ce-doped In₂O₃ dispersed in nonpolar solvents with different refractive indices. Inset: LSPR peak wavelength versus refractive index.

stable and highly crystalline nanocrystals with narrow MIR LSPR absorption, though LSPR peak shape and nanocrystal shape depended on the amount and type of cerium precursor used. For example, nanocrystals synthesized with Ce-acac tended to adopt cubic shapes with (100)-terminated facets, while those synthesized with Ce-TMHD were pseudospherical. As we show below, consistent with previously published simulations of ICO nanocrystals,¹³ the synthesis of nanocrystals in shapes with defined corners and edges has positive implications for near-field enhancement.

Liquid-cell Fourier transform infrared (FTIR) spectra of Ce:In₂O₃ nanocrystals dispersed in tetrachloroethylene display remarkably narrow LSPR peaks that are air-stable (Figure 2a). The peak energy increases with Ce content, indicating donor dopant behavior. The UV optical bandgap shifts systematically to higher energy with increased doping (Figure 2b) as free conduction band electrons populate band edge states in accordance with observations of the Burstein–Moss effect in other doped oxide nanocrystals.^{1,2} Dispersing the nanocrystals in nonpolar solvents with increasing refractive index results in a systematic redshift in LSPR peak position (Figure 2c). When the wavelength of the extinction peak is plotted versus refractive index (Figure 2c inset), a linear trend is observed, consistent with the expected sensitivity of LSPR to the dielectric environment. These LSPR peaks are exceptionally narrow and symmetric, especially compared to Sn:In₂O₃ nanocrystals with LSPR in the same spectral region (Figure 2a). The narrowest peak occurs for nanocrystals doped with 5.2% Ce, which display an LSPR peak at 2522 cm^{−1} with a width of only 621 cm^{−1} (77 meV) for a quality factor of 4.08. To our knowledge, this is higher than the *Q* values for gold nanostructures, nitrides, chalcogenides, and other doped metal oxide nanocrystals with LSPR in or approaching this spectral region.^{1,2,4,7,14–22} Furthermore, these peak widths are among the narrowest reported for any plasmonic nanoparticle, including single gold nanoparticles (120 meV),²³ Sn:In₂O₃ (113 meV),⁷ and ICO codoped with fluorine (59 meV).²⁴

Narrow and symmetric LSPR peaks indicate low levels of electronic damping and ionized impurity scattering.^{4,7} To quantify these electronic properties, we performed fits to the FTIR spectra with an extended Drude model using a MATLAB code developed by our group.^{7,25–27} In contrast to a simple Drude approximation, our model employs an empirical frequency-dependent damping function ($\Gamma(\omega)$ in eq 1) to account for the frequency dependence of ionized impurity scattering:

$$\Gamma(\omega) = \Gamma_L - \frac{\Gamma_L - \Gamma_H}{\pi} \left[\tan^{-1} \left(\frac{\omega - \Gamma_X}{\Gamma_W} \right) + \frac{\pi}{2} \right] \quad (2)$$

where Γ_L is a low-frequency damping constant, Γ_H is a high-frequency damping constant, Γ_X is a crossover frequency between the low-frequency and high-frequency damping regimes, and Γ_W is the width of the crossover region.²⁸ The magnitude of the low-frequency damping constant captures the influence of ionized impurity scattering, and when $\Gamma_L \gg \Gamma_H$ frequency-dependent ionized impurity scattering is a dominant LSPR damping mechanism. At sufficiently low frequencies, oscillating electrons effectively feel the same scattering potentials as they would under a DC field, so fits to the spectra can be used to calculate optical DC electronic mobility by the following relationships⁷

$$\sigma_{\text{opt}} = en\mu_{\text{opt}} = \frac{ne^2}{m^*\Gamma(0)} \quad (3)$$

where σ_{opt} is the optically derived electronic conductivity, μ_{opt} is the optically derived electron mobility, n is the free carrier concentration, m^* is the effective mass of an electron, and $\Gamma(0)$ is the value of the damping function (eq 2) at zero frequency. Electronic properties derived optically by this method have been found to match physically measured properties, including mobility, in both dense thin films and electronically connected nanocrystalline films.^{26,29–31}

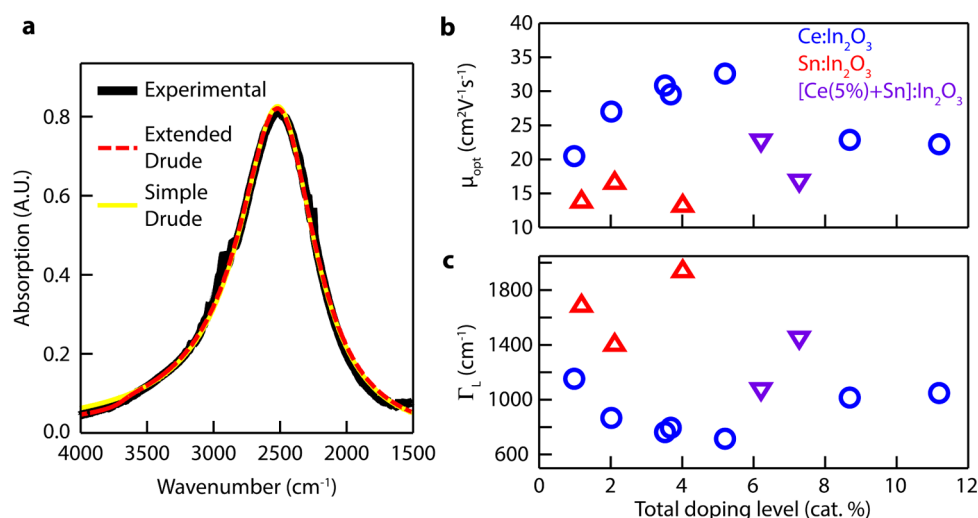


Figure 3. Drude modeling of LSPR in Ce:In₂O₃ nanocrystals. (a) Example extended and simple Drude model fits to the FTIR spectrum of 5.2% Ce:In₂O₃ nanocrystals. (b) Optically calculated electronic mobility of Ce:In₂O₃ (blue circles), Sn:In₂O₃ (red triangles), and Ce/Sn-codoped In₂O₃ nanocrystals (purple, inverted triangles) versus doping level. (c) Low-frequency damping constant, calculated with the extended Drude model, for Ce:In₂O₃, Sn:In₂O₃, and Ce/Sn-codoped In₂O₃ nanocrystals versus doping level.

We calculated the plasma frequency, electron concentration, damping constants, and electronic mobility for Ce:In₂O₃ nanocrystals and compared them to Sn:In₂O₃ nanocrystals containing 1 to 4% Sn. A representative fit and the salient fitting results are shown in Figure 3 and Table S1. The remaining Drude fits are shown in Figure S3. In Ce:In₂O₃, the crossover frequencies are significantly blueshifted relative to the LSPR peak energy with narrow crossover widths and low Γ_L values. This is indicative of damping by a frequency-independent constant throughout the bandwidth of the LSPR peak and suppressed ionized impurity scattering.⁷ When we fit the spectra using a simple Drude model with constant damping, the fits were nearly identical (Figure 3a, Table S2), supporting this conclusion. Figures 2a and S3 show a limited blueshift in the LSPR peak at doping levels higher than 5.2%, suggesting diminished donor character at higher Ce concentration. This is in contrast to Sn:In₂O₃, which has a stronger LSPR blueshift with Sn content. Comparing the electron concentrations determined by Drude analysis to Ce concentration reveals that a significant number of dopants are not activated as donors (Figure S4), as is typical for degenerately doped metal oxides. X-ray absorption spectroscopy (XAS) revealed that a significant fraction of Ce dopants were not ionized, which is most likely a consequence of cerium's facile transition between the 3+ and 4+ oxidation states. We note that more complex defect chemistries are also possible and may be consuming free electrons, because the electron concentrations were generally lower than expected based on the Ce⁴⁺ fraction determined by XAS. For example, defect clustering between dopants and oxygen interstitials is a well-known phenomenon in bulk Sn:In₂O₃³² and has been observed in plasmonic Sn:In₂O₃ nanocrystals.³³ Similar defect equilibria may also contribute to limited activation at higher doping levels in Ce:In₂O₃.

The values for μ_{opt} and Γ_L (Figure 3b,c) underscore the exceptional electronic properties of Ce:In₂O₃. Both the low- and high-frequency damping constants are significantly lower than for Sn:In₂O₃ nanocrystals, and the 2.0–5.2% Ce-doped samples outperform our previously reported best performance from 6.4% Sn-doped In₂O₃ ($\Gamma_L = 913 \text{ cm}^{-1}$).⁷ We also confirmed the deleterious effects of tin doping by preparing

Ce/Sn-codoped samples; incorporation of only 1%–2% Sn significantly decreased mobility and increased both the low- and high-frequency damping constants (Figure 3b,c), but these nanocrystals nevertheless displayed enhanced properties relative to nanocrystals doped with tin only. In particular, the low Γ_L values quantitatively describe how ionized impurity scattering is suppressed in Ce:In₂O₃ compared to Sn:In₂O₃. Furthermore, the extracted frequency-dependent damping functions translate to high electronic mobility as calculated by eq 3; we calculated mobilities up to $33 \text{ cm}^2 \text{ V}^{-1} \text{ s}^{-1}$, twice what we observed for Sn:In₂O₃ nanocrystals.

The observed mobility trends suggest that cerium incorporation suppresses ionized impurity scattering by influencing crystal structure, electronic structure, or both. Furthermore, the electronic mobility in Ce:In₂O₃ actually increases substantially with doping level up to 5.2% Ce. These results are contrary to conventional models of ionized impurity scattering, which predict a decrease in mobility with doping.^{6,34} To evaluate the microscopic origins of the electronic property enhancements, we performed density functional theory (DFT) calculations using the Vienna *ab initio* simulation package (VASP) to simulate local strains, defect formation energies, and electronic structure in Ce:In₂O₃.^{35–38} In all calculations, doping was simulated by replacing a Wyckoff 8b In site with Ce or Sn.

Using a GGA+U exchange correlation functional, we first calculated radial strains surrounding an oxygen vacancy, a substitutional Ce dopant, and a substitutional Sn dopant in a 80-atom In₂O₃ bixbyite unit cell, corresponding to a cation doping level of 3.1% (Figure S5).³⁹ The magnitude of the nearest neighbor strain around cerium ($\sim 4\%$) is slightly lower than tin ($\sim 5\%$). This slight decrease in lattice distortion is probably not the primary driver of high mobility, though it may be responsible for some decrease in frequency-independent electron–phonon scattering. By contrast, the strain around an oxygen vacancy is up to three times greater and decays over a longer distance, which would cause strong electron–phonon scattering through lattice distortion. Furthermore, the ionized impurity scattering potentials from ionized oxygen vacancies are strongly felt by free electrons due to the significant contribution of oxygen orbitals to the conduction band.^{8,40}

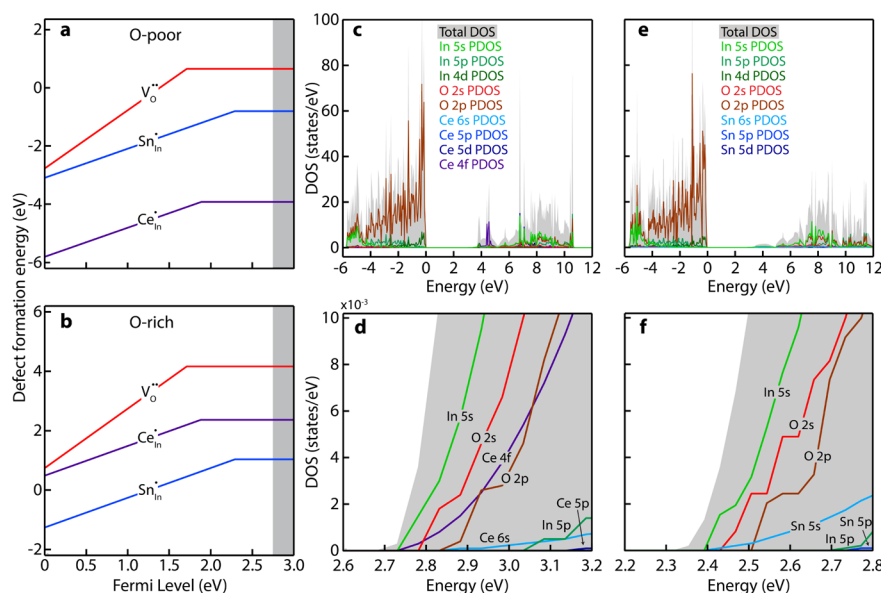


Figure 4. DFT calculations on Ce:In₂O₃ and Sn:In₂O₃. (a) Defect formation energies versus Fermi level for oxygen vacancies ($V_O^{\bullet\bullet}$), substitutional tin dopants (Sn_{In}^{\bullet}), and substitutional cerium dopants (Ce_{In}^{\bullet}) under oxygen-poor conditions. The valence band maximum is set to 0 eV and the gray-shaded region denotes the conduction band edge. The slope of the formation energy versus Fermi level reflects the stable charge state of the defect at that Fermi level. (b) Defect formation energies versus Fermi level under oxygen-rich conditions. (c) Total and partial density of states for a 40 atom primitive In₂O₃ unit cell containing one substitutional Ce dopant. The valence band maximum is set to 0 eV. (d) Detailed view of the total and partial DOS at the conduction band edge for Ce:In₂O₃. (e) Total and partial density of states for a 40 atom primitive In₂O₃ unit cell containing one substitutional Sn dopant. (f) Detailed view of the total and partial DOS at the conduction band edge for Sn:In₂O₃.

Considering strong electron scattering by oxygen vacancies, the incorporation of Ce might suppress ionized impurity scattering by reducing the equilibrium concentration of oxygen vacancies. We therefore used DFT to calculate the defect formation energies for an oxygen vacancy, a substitutional cerium dopant, and a substitutional tin dopant in a bixbyite unit cell according to the following equation

$$E_{\text{defect}}[X^q] = E_{\text{DFT}}[X^q] - E_{\text{DFT}}[\text{bulk}] - \sum_i n_i \mu_i + qE_F + E_{\text{corr}} \quad (4)$$

where $E_{\text{defect}}[X^q]$ is the formation energy of a defect X with charge q , $E_{\text{DFT}}[X^q]$ is the total energy of the defective cell calculated by DFT, $E_{\text{DFT}}[\text{bulk}]$ is the total energy of the perfect cell, n_i and μ_i are the number and chemical potential, respectively, of the atoms added or subtracted from the cell to form the defect, E_F is the Fermi level relative to the valence band maximum, and E_{corr} is a correction factor that accounts for potential alignment and image charges of the defect that arise during DFT calculations.⁴¹ This treatment captures the dependence of defect formation energies on the Fermi level as well as the chemical potential of oxygen, allowing us to display these energies as a function of E_F under oxygen-poor and -rich conditions (see SI for a more detailed explanation). We note that the oxygen-poor case, corresponding to the minimum chemical potential of oxygen for which In₂O₃ is stable with respect to decomposition into indium metal and O₂, likely matches our anaerobic synthetic environment more closely, especially considering the precipitation of bulk metal observed in some similarly performed nanocrystal syntheses.^{21,42,43}

We calculated defect formation energies for oxygen vacancies and substitutional tin in both the oxygen-poor (Figure 4a) and oxygen-rich (Figure 4b) limits, and they agree well with previous computational studies.^{44,45} Our calculations also

indicate that under oxygen-poor conditions, the formation of substitutional Ce defects is significantly more energetically favorable than substitutional tin or oxygen vacancies, which have comparable formation energies. The energy difference between substitutional Ce and Sn arises primarily from the $E_{\text{DFT}}[X^q]$ term, the energy of a unit cell with one Ce defect is about 3.5 eV lower than a unit cell with one Sn defect, while the chemical potential and correction terms in eq 4 differ by 0.5 eV or less between Ce and Sn doping. Incorporation of Ce or Sn donors increases the Fermi level, which consequently increases the formation energy of oxygen vacancies by over 3 eV as the Fermi level reaches the CBM. For a given electron concentration, it is much more energetically favorable to compensate free electrons with Ce donors as opposed to oxygen vacancies. In Sn:In₂O₃, the energy difference between substitutional Sn and oxygen vacancies is significantly smaller, so free electrons would more likely be compensated by a mix of both defects. Figure 4a also shows that neutral defects become favorable at higher Fermi levels, indicating the presence of both ionized and neutral dopants, which agrees with our observation of partial dopant activation. Overall, when comparing Ce:In₂O₃ and Sn:In₂O₃ at the same electron concentration, our results suggest that oxygen vacancies may be more prominent in the latter. This interpretation is consistent with our observations that the electronic mobility in Ce:In₂O₃ nanocrystals increases significantly with Ce concentration, while the electronic mobility in Sn:In₂O₃ nanocrystals does not increase with Sn doping.

The formation energies of Ce and Sn substitutional defects change progressively with oxygen chemical potential, eventually crossing over so that Sn is more favorable than Ce at oxygen-rich conditions (where the chemical potential of oxygen is set equal to the energy of O in an O₂ molecule, Figure 4b). This manifests at high oxygen activity because CeO₂ has a significantly lower chemical potential than SnO₂ (by about

5 eV, see Tables S3 and S4); the chemical potentials of these two oxides set the oxygen-rich boundary conditions for eq 4 and under these conditions the chemical potential difference overwhelms the difference in the $E_{\text{DFT}}[X^q]$ term. Between these two extremes of oxygen chemical potential, substitutional Ce remains more favorable (Figure S6). At the oxygen-rich extreme, the formation energy for all three defects is positive over nearly the whole range of Fermi levels, indicating that n-type doping would be difficult under these conditions. These conditions are unlikely to be encountered experimentally, and high oxygen partial pressures are associated with other deleterious effects in $\text{Sn:In}_2\text{O}_3$, such as defect clusters of tin and oxygen interstitials, which consume free electrons upon formation.³²

Finally, we considered electronic structure as an explanation for low ionized impurity scattering in $\text{Ce:In}_2\text{O}_3$. Because Ce is significantly more electropositive than In, hybridization between dopant orbitals and the states near the CBM should be limited. To test this hypothesis, we used DFT to calculate the electronic density of states (DOS) for a 40 atom primitive bixbyite unit cell with one substitutional Ce or Sn dopant, which corresponds to a doping level of 6.3% (Figure 4c,d). Here, we used the HSE06 hybrid functional to obtain a more accurate description of electronic structure, faithfully reproducing indium oxide's fundamental bandgap of 2.7 eV.^{40,46–48} We also calculated the DOS of $\text{Sn:In}_2\text{O}_3$ (Figure 4e,f) and stoichiometric In_2O_3 for comparison (Figure S7). The partial density of states (PDOS) reveal that the bottom of the conduction band is primarily of In 5s and O 2s character, which implies a wide and dispersive conduction band that facilitates high electron mobility. The only dopant states that overlap in energy with the bottom of the conduction band are Ce 4f states, which are highly localized states that should resist mixing with s and p orbitals. The Ce 6s and 5p states, which could hybridize more strongly, contribute no PDOS to the CBM and only become significant about 1 eV above the band edge. By contrast, Sn 5s states are present at the CBM in our $\text{Sn:In}_2\text{O}_3$ calculations, and previous studies have shown strong hybridization between these and In 5s orbitals.^{8,49} Optical bandgap measurements (Figure 2b) suggest that the Fermi level for the 5.2% Ce-doped sample (with the highest mobility) is about 0.2 eV above the CBM or about 2.9 eV above the valence band edge. Electrons near the Fermi level that contribute to conductivity and LSPR are thus unlikely to interact substantially with the Ce dopants, while they interact strongly with Sn dopants.

In effect, the electronic structure of $\text{Ce:In}_2\text{O}_3$ is such that the dopant ions are effectively electrostatically screened and are not expected to strongly scatter free electrons. Moving electrons in $\text{Ce:In}_2\text{O}_3$ effectively experience the same electronic potentials as they would in intrinsic In_2O_3 due to this remote screening, limiting ionized impurity scattering in a manner analogous to modulation doping, where ionized dopants are spatially separated from conducting electrons.⁵⁰ Here, the electronic separation in energy and/or orbital shape of dopant levels from the conduction states suppresses ionized impurity scattering and is likely the primary driver of enhanced mobility. Combined with our defect calculations, which suggest reduced oxygen vacancy concentrations with Ce doping, these electronic structure effects explain why we observe such narrow LSPR peaks and high electronic mobilities in $\text{Ce:In}_2\text{O}_3$ nanocrystals.

On the basis of their exceptional LSPR properties, we set out to evaluate the potential of $\text{Ce:In}_2\text{O}_3$ nanocrystals for near-field

enhancement applications. We measured absorption spectra of single nanocrystals using synchrotron infrared nanospectroscopy (SINS, Figure 5a), which utilizes near-field concentration

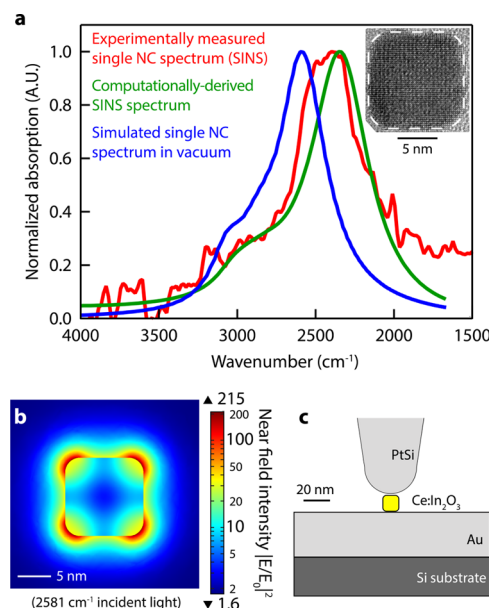


Figure 5. LSPR properties of $\text{Ce:In}_2\text{O}_3$ single nanocrystals. (a) Experimentally collected SINS spectrum (red line) of a single cubic nanocrystal with 5.2% Ce, simulated SINS spectrum (green line) used to determine the dielectric function and simulate the absorption spectrum (blue line) of a single isolated nanocrystal. Inset: TEM of the nanocrystal used as a model. (b) Simulated near-field intensity map of the model nanocrystal illuminated at the LSPR peak frequency. (c) Depiction of the geometry used to model and discretize the coupled substrate–nanocrystal–tip system in the SINS experiment (drawn to scale except for the thickness of the Si substrate).

of light by a metallic AFM tip positioned just above an isolated nanoscale object (Figure 5c) to collect an FTIR spectrum of that object.⁵¹ Our group has recently pioneered the use of this technique to interrogate single $\text{Sn:In}_2\text{O}_3$ and AZO nanocrystals in order to measure LSPR properties without the influence of ensemble peak broadening due to size, shape, or dopant heterogeneity.⁵² We collected SINS spectra (which can effectively correspond to absorption spectra)⁵³ of several individual cubic-shaped $\text{Ce:In}_2\text{O}_3$ nanocrystals with average 5.2% Ce (Figures 5a and S8) and observed line widths as narrow as 479 cm^{-1} (59 meV), corresponding to a quality factor of 5.5 for a single nanocrystal, compared to 4.08 for the ensemble, meaning that some peak broadening is the result of inhomogeneous broadening. This result highlights the plasmonic performance of $\text{Ce:In}_2\text{O}_3$ nanocrystals and the usefulness of SINS; the plasmonic damping in this material is actually nearly 25% less than ensemble measurements suggest.

To simulate near-field enhancement around a nanocrystal, it is necessary to know its frequency-dependent dielectric function (eq 1). Here, we use the SINS spectrum of a single, isolated nanocrystal to extract a materials-specific dielectric function free of effective medium complications and artifacts that would arise from ensemble peak broadening. Experimental SINS spectra contain the scattering and absorption properties of a coupled PtSi| $\text{Ce:In}_2\text{O}_3$ |Au (tip–nanocrystal–substrate) system; to accurately generate a dielectric function for the $\text{Ce:In}_2\text{O}_3$ nanocrystal free of tip or substrate influence, we

computationally solved Maxwell's equations for this system using the finite element method (COMSOL multiphysics program) to discretize each component. Using our ensemble Drude model fit as an initial guess for the nanocrystal dielectric function, along with known dielectric functions for PtSi and Au, we simulated the SINS spectrum and iteratively adjusted the plasma frequency and damping functions in the dielectric function until the simulated spectrum matched the experimentally measured spectrum (Figures 5a, S9). The dielectric function of the nanocrystal, estimated as such, allowed us to simulate the absorption, scattering, and near-field properties of an isolated nanocrystal without tip or substrate influence.

We simulated the enhancement of incident light electric field intensity around a cubic Ce:In₂O₃ nanocrystal by using the dielectric function to solve Maxwell's equations throughout the discretized nanocrystal (Figure 5b). Incident light, polarized along one of the cube axes and with a frequency of 2581 cm⁻¹, excites a dipolar LSPR mode with a maximum near-field intensity enhancement factor of 215 relative to the incident intensity. The electric-field and near-field enhancement maps of other modes are shown in Figure S10. The benefits of nanocrystal shape control are clear, as the near-field enhancement is strongest near the cube vertices, and simulated near-field enhancement factors around a spherical Ce:In₂O₃ nanocrystal reached only 81 (Figure S11). These simulations underscore the advantages of low loss Ce:In₂O₃ nanocrystals for field-enhancement applications like SEIRA.

We have shown here that by purposefully choosing a dopant that minimizes ionized impurity scattering, doped metal oxide nanocrystals can exhibit high electronic mobilities, very narrow LSPR peaks, and strong near-field enhancement. The predicted near-field performance of Ce:In₂O₃ nanocrystals points to their potential for applications that rely on intense light concentration well below the diffraction limit. Ce:In₂O₃ nanocrystals would be good candidates for SEIRA substrates, where they could be tuned to resonantly couple to and enhance molecular vibration signals throughout the MIR for spectroscopy or sensing applications. From an application perspective, the colloidal nature of Ce:In₂O₃ provides a distinct advantage: many of the other recently described systems with MIR plasmons, including nanostructured Sn:In₂O₃ thin films,⁵⁴ patterned graphene,⁵⁵ doped silicon nanowires,⁵⁶ or gold antenna arrays,⁵⁷ require complex lithography or other nanostructuring techniques that limit options for their integration in different environments and effectively preclude large scale applications. In contrast, colloidal nanocrystals are readily dispersed in fluid environments or on substrates and can be made to self-assemble into superlattices^{58–60} (with plasmonic hotspots between nanocrystals⁶¹), and colloidal synthesis has been demonstrated as a scalable technique.⁶²

We hope that this report spurs additional research and development of Ce:In₂O₃, specifically. On the basis of our results, Ce:In₂O₃ offers a rich platform for studying the interplay between synthesis, defect chemistry, electronic properties, and performance. For example, Ce:In₂O₃ thin films would be particularly useful for transparent conductor applications that require low carrier concentration and high mobility, such as thin film photovoltaics.⁶ Finally, the strategies incorporated here, rational dopant selection and defect engineering, could be applied to manipulate the electronic and plasmonic properties of any number of doped metal oxides. This suggestion comes at a time that growing efforts are underway to discover new transparent conductors incorporat-

ing unusual dopants,^{8,9} multiple elements,^{63,64} or correlated electron metals.⁶⁵ To advance the understanding and control of LSPR in doped oxide nanocrystals, we plan to extend this strategy to study the influence of alternative dopants on the LSPR properties in other metal oxide hosts like TiO₂, ZnO, and SnO₂.

■ ASSOCIATED CONTENT

§ Supporting Information

The Supporting Information is available free of charge on the ACS Publications website at DOI: 10.1021/acs.nanolett.6b01171.

Details of nanocrystal synthesis, sample characterization and analysis (TEM, XRD, FTIR, UV-vis), details of Drude modeling and analysis with additional discussion, details of XAS characterization and additional discussion, details of DFT calculations and analysis along with additional discussion, details of SINS single-nanocrystal measurements, and details and additional discussion of near-field simulations. (PDF)

■ AUTHOR INFORMATION

Corresponding Author

*E-mail: milliron@che.utexas.edu.

Notes

The authors declare no competing financial interest.

■ ACKNOWLEDGMENTS

This work was supported by a U.S. Department of Energy (DOE) ARPA-E Grant (E.L.R., A.B., A.A., R.W.J., C.J.D., D.J.M.) and the Welch Foundation (A.A., D.J.M.; Grant F-1848), and The Norwegian High-Performance Computing Consortium (NOTUR) under Project No. NN9264K (A.B., S.M.S.). Additional support was provided by National Science Foundation (NSF) Graduate Student Research Fellowships (A.B., C.J.D.) under Grant DGE 1106400 and by the NSF Graduate Research Opportunities Worldwide (GROW) program (A.B.). A.S. was supported by the Bay Area Photovoltaics Consortium, sponsored by DOE EERE. E.L.R. and A.B. also acknowledge support from the UC Berkeley Chancellor's Fellowship. SINS measurements were performed on beamline 1.4.4. at the Advanced Light Source (ALS) at Lawrence Berkeley National Lab (LBNL). R.W.J. was additionally supported by an ALS Doctoral Fellowship in Residence. The authors acknowledge the efforts of Hans Bechtel and Markus Raschke in developing the SINS instrument and for assistance in its operation. XAS experiments were performed on beamlines 8.0.1 and 6.3.2 at the ALS. The ALS and Molecular Foundry at LBNL supported this work as user facilities funded by the Office of Science, Office of Basic Energy Sciences, of the DOE under contract DE-AC02-05CH11231.

■ REFERENCES

- (1) Buonsanti, R.; Llordés, A.; Aloni, S.; Helms, B. A.; Milliron, D. J. Tunable Infrared Absorption and Visible Transparency of Colloidal Aluminum-Doped Zinc Oxide Nanocrystals. *Nano Lett.* **2011**, *11*, 4706–4710.
- (2) Gordon, T. R.; Paik, T.; Klein, D. R.; Naik, G. V.; Caglayan, H.; Boltasseva, A.; Murray, C. B. Shape-Dependent Plasmonic Response and Directed Self-Assembly in a New Semiconductor Building Block,

Indium-Doped Cadmium Oxide (ICO). *Nano Lett.* **2013**, *13*, 2857–2863.

(3) Choi, S.-I.; Nam, K. M.; Park, B. K.; Seo, W. S.; Park, J. T. Preparation and Optical Properties of Colloidal, Monodisperse, and Highly Crystalline ITO Nanoparticles. *Chem. Mater.* **2008**, *20*, 2609–2611.

(4) Lounis, S. D.; Runnerstrom, E. L.; Llordés, A.; Milliron, D. J. Defect Chemistry and Plasmon Physics of Colloidal Metal Oxide Nanocrystals. *J. Phys. Chem. Lett.* **2014**, *5*, 1564–1574.

(5) Hamberg, I.; Granqvist, C. G. Evaporated Sn-Doped In_2O_3 Films: Basic Optical Properties and Applications to Energy-Efficient Windows. *J. Appl. Phys.* **1986**, *60*, R123.

(6) Ellmer, K. Past Achievements and Future Challenges in the Development of Optically Transparent Electrodes. *Nat. Photonics* **2012**, *6*, 809–817.

(7) Lounis, S. D.; Runnerstrom, E. L.; Bergerud, A.; Nordlund, D.; Milliron, D. J. Influence of Dopant Distribution on the Plasmonic Properties of Indium Tin Oxide Nanocrystals. *J. Am. Chem. Soc.* **2014**, *136*, 7110–7116.

(8) Bhachu, D. S.; Scanlon, D. O.; Sankar, G.; Veal, T. D.; Egdel, R. G.; Cibin, G.; Dent, A. J.; Knapp, C. E.; Carmalt, C. J.; Parkin, I. P. Origin of High Mobility in Molybdenum-Doped Indium Oxide. *Chem. Mater.* **2015**, *27*, 2788–2796.

(9) Sachet, E.; Shelton, C. T.; Harris, J. S.; Gaddy, B. E.; Irving, D. L.; Curtarolo, S.; Donovan, B. F.; Hopkins, P. E.; Sharma, P. A.; Sharma, A. L.; et al. Dysprosium-Doped Cadmium Oxide as a Gateway Material for Mid-Infrared Plasmonics. *Nat. Mater.* **2015**, *14*, 414–420.

(10) Shannon, R. D. Revised Effective Ionic Radii and Systematic Studies of Interatomic Distances in Halides and Chalcogenides. *Acta Crystallogr., Sect. A: Cryst. Phys., Diff., Theor. Gen. Crystallogr.* **1976**, *32*, 751–767.

(11) Kang, S.; Cho, S.; Song, P. Effect of Cerium Doping on the Electrical Properties of Ultrathin Indium Tin Oxide Films for Application in Touch Sensors. *Thin Solid Films* **2014**, *559*, 92–95.

(12) Kobayashi, E.; Watabe, Y.; Yamamoto, T. High-Mobility Transparent Conductive Thin Films of Cerium-Doped Hydrogenated Indium Oxide. *Appl. Phys. Express* **2015**, *8*, 015505.

(13) Agrawal, A.; Kriegel, I.; Milliron, D. J. Shape-Dependent Field Enhancement and Plasmon Resonance of Oxide Nanocrystals. *J. Phys. Chem. C* **2015**, *119*, 6227–6238.

(14) Prodan, E.; Nordlander, P.; Halas, N. J. Electronic Structure and Optical Properties of Gold Nanoshells. *Nano Lett.* **2003**, *3*, 1411–1415.

(15) Sando, G. M.; Berry, A. D.; Campbell, P. M.; Baronavski, A. P.; Owrutsky, J. C. Surface Plasmon Dynamics of High-Aspect-Ratio Gold Nanorods. *Plasmonics* **2007**, *2*, 23–29.

(16) Guler, U.; Naik, G. V.; Boltasseva, A.; Shalae, V. M.; Kildishev, A. V. Performance Analysis of Nitride Alternative Plasmonic Materials for Localized Surface Plasmon Applications. *Appl. Phys. B: Lasers Opt.* **2012**, *107*, 285–291.

(17) Cooper, C. T.; Rodriguez, M.; Blair, S.; Shumaker-Parry, J. S. Mid-Infrared Localized Plasmons Through Structural Control of Gold and Silver Nanocrescents. *J. Phys. Chem. C* **2015**, *119*, 11826–11832.

(18) Luther, J. M.; Jain, P. K.; Ewers, T.; Alivisatos, A. P. Localized Surface Plasmon Resonances Arising From Free Carriers in Doped Quantum Dots. *Nat. Mater.* **2011**, *10*, 361–366.

(19) Manthiram, K.; Alivisatos, A. P. Tunable Localized Surface Plasmon Resonances in Tungsten Oxide Nanocrystals. *J. Am. Chem. Soc.* **2012**, *134*, 3995–3998.

(20) Mattox, T. M.; Bergerud, A.; Agrawal, A.; Milliron, D. J. Influence of Shape on the Surface Plasmon Resonance of Tungsten Bronze Nanocrystals. *Chem. Mater.* **2014**, *26*, 1779–1784.

(21) Diroll, B. T.; Gordon, T. R.; Gauding, E. A.; Klein, D. R.; Paik, T.; Yun, H. J.; Goodwin, E. D.; Damodhar, D.; Kagan, C. R.; Murray, C. B. Synthesis of N-Type Plasmonic Oxide Nanocrystals and the Optical and Electrical Characterization of Their Transparent Conducting Films. *Chem. Mater.* **2014**, *26*, 4579–4588.

(22) De Trizio, L.; Buonsanti, R.; Schimpf, A. M.; Llordés, A.; Gamelin, D. R.; Simonutti, R.; Milliron, D. J. Nb-Doped Colloidal

TiO_2 Nanocrystals with Tunable Infrared Absorption. *Chem. Mater.* **2013**, *25*, 3383–3390.

(23) Klar, T.; Perner, M.; Grosse, S.; von Plessen, G.; von, G.; Spirkel, W.; Feldmann, J. Surface-Plasmon Resonances in Single Metallic Nanoparticles. *Phys. Rev. Lett.* **1998**, *80*, 4249–4252.

(24) Ye, X.; Fei, J.; Diroll, B. T.; Paik, T.; Murray, C. B. Expanding the Spectral Tunability of Plasmonic Resonances in Doped Metal-Oxide Nanocrystals Through Cooperative Cation-Anion Codoping. *J. Am. Chem. Soc.* **2014**, *136*, 11680–11686.

(25) Garcia, G.; Buonsanti, R.; Runnerstrom, E. L.; Mendelsberg, R. J.; Llordés, A.; Anders, A.; Richardson, T. J.; Milliron, D. J. Dynamically Modulating the Surface Plasmon Resonance of Doped Semiconductor Nanocrystals. *Nano Lett.* **2011**, *11*, 4415–4420.

(26) Mendelsberg, R. J.; Garcia, G.; Milliron, D. J. Extracting Reliable Electronic Properties From Transmission Spectra of Indium Tin Oxide Thin Films and Nanocrystal Films by Careful Application of the Drude Theory. *J. Appl. Phys.* **2012**, *111*, 063515.

(27) Mendelsberg, R. J.; Garcia, G.; Li, H.; Manna, L.; Milliron, D. J. Understanding the Plasmon Resonance in Ensembles of Degenerately Doped Semiconductor Nanocrystals. *J. Phys. Chem. C* **2012**, *116*, 12226–12231.

(28) Mergel, D.; Qiao, Z. Dielectric Modelling of Optical Spectra of Thin $\text{In}_2\text{O}_3/\text{Sn}$ Films. *J. Phys. D: Appl. Phys.* **2002**, *35*, 794–801.

(29) Qiao, Z.; Agashe, C.; Mergel, D. Dielectric Modeling of Transmittance Spectra of Thin $\text{ZnO}:\text{Al}$ Films. *Thin Solid Films* **2006**, *496*, 520–525.

(30) Solieman, A.; Aegerter, M. A. Modeling of Optical and Electrical Properties of $\text{In}_2\text{O}_3/\text{Sn}$ Coatings Made by Various Techniques. *Thin Solid Films* **2006**, *502*, 205–211.

(31) Steinhauser, J.; Fay, S.; Oliveira, N.; Vallat-Sauvain, E.; Ballif, C. Transition Between Grain Boundary and Intragrain Scattering Transport Mechanisms in Boron-Doped Zinc Oxide Thin Films. *Appl. Phys. Lett.* **2007**, *90*, 142107.

(32) Frank, G.; Köstlin, H. Electrical Properties and Defect Model of Tin-Doped Indium Oxide Layers. *Appl. Phys. A: Solids Surf.* **1982**, *27*, 197–206.

(33) Shanker, G. S.; Tandon, B.; Shibata, T.; Chattopadhyay, S.; Nag, A. Doping Controls Plasmonics, Electrical Conductivity, and Carrier-Mediated Magnetic Coupling in Fe and Sn Codoped In_2O_3 Nanocrystals: Local Structure Is the Key. *Chem. Mater.* **2015**, *27*, 892–900.

(34) Chattopadhyay, D.; Queisser, H. J. Electron Scattering by Ionized Impurities in Semiconductors. *Rev. Mod. Phys.* **1981**, *53*, 745–768.

(35) Hohenberg, P.; Kohn, W. Inhomogeneous Electron Gas. *Phys. Rev.* **1964**, *136*, B864–B871.

(36) Kohn, W.; Sham, L. J. Self-Consistent Equations Including Exchange and Correlation Effects. *Phys. Rev.* **1965**, *140*, A1133–A1138.

(37) Kresse, G.; Hafner, J. Ab Initio Molecular Dynamics for Liquid Metals. *Phys. Rev. B: Condens. Matter Mater. Phys.* **1993**, *47*, 558–561.

(38) Kresse, G.; Furthmüller, J. Efficiency of Ab-Initio Total Energy Calculations for Metals and Semiconductors Using a Plane-Wave Basis Set. *Comput. Mater. Sci.* **1996**, *6*, 15–50.

(39) Perdew, J.; Burke, K.; Ernzerhof, M. Generalized Gradient Approximation Made Simple. *Phys. Rev. Lett.* **1996**, *77*, 3865–3868.

(40) Walsh, A.; Da Silva, J. L. F.; Wei, S.-H.; Körber, C.; Klein, A.; Piper, L. F. J.; DeMasi, A.; Smith, K. E.; Panaccione, G.; Torelli, P.; et al. Nature of the Band Gap of In_2O_3 Revealed by First-Principles Calculations and X-Ray Spectroscopy. *Phys. Rev. Lett.* **2008**, *100*, 167402.

(41) Freysoldt, C.; Grabowski, B.; Hickel, T.; Neugebauer, J.; Kresse, G.; Janotti, A.; Van de Walle, C. G. First-Principles Calculations for Point Defects in Solids. *Rev. Mod. Phys.* **2014**, *86*, 253–305.

(42) Steckel, J. S.; Yen, B. K. H.; Oertel, D. C.; Bawendi, M. G. On the Mechanism of Lead Chalcogenide Nanocrystal Formation. *J. Am. Chem. Soc.* **2006**, *128*, 13032–13033.

- (43) Owen, J. S.; Chan, E. M.; Liu, H.; Alivisatos, A. P. Precursor Conversion Kinetics and the Nucleation of Cadmium Selenide Nanocrystals. *J. Am. Chem. Soc.* **2010**, *132*, 18206–18213.
- (44) Agoston, P.; Erhart, P.; Klein, A.; Albe, K. Geometry, Electronic Structure and Thermodynamic Stability of Intrinsic Point Defects in Indium Oxide. *J. Phys.: Condens. Matter* **2009**, *21*, 455801.
- (45) Chen, Z.; Huang, L.; Zhang, Q.; Xi, Y.; Li, R.; Li, W.; Xu, G.; Cheng, H. Electronic Structures and Transport Properties of N-Type-Doped Indium Oxides. *J. Phys. Chem. C* **2015**, *119*, 4789–4795.
- (46) Bourlange, A.; Payne, D. J.; Egdel, R. G.; Foord, J. S.; Edwards, P. P.; Jones, M. O.; Schertel, A.; Dobson, P. J.; Hutchison, J. L. Growth of In_2O_3 (100) on Y-Stabilized ZrO_2 (100) by O-Plasma Assisted Molecular Beam Epitaxy. *Appl. Phys. Lett.* **2008**, *92*, 092117.
- (47) Heyd, J.; Scuseria, G. E.; Ernzerhof, M. Hybrid Functionals Based on a Screened Coulomb Potential. *J. Chem. Phys.* **2003**, *118*, 8207.
- (48) Krukau, A. V.; Vydrov, O. A.; Izmaylov, A. F.; Scuseria, G. E. Influence of the Exchange Screening Parameter on the Performance of Screened Hybrid Functionals. *J. Chem. Phys.* **2006**, *125*, 224106.
- (49) Walsh, A.; Da Silva, J. L. F.; Wei, S.-H. Origins of Band-Gap Renormalization in Degenerately Doped Semiconductors. *Phys. Rev. B: Condens. Matter Mater. Phys.* **2008**, *78*, 075211.
- (50) Pfeiffer, L.; West, K. W.; Stormer, H. L.; Baldwin, K. W. Electron Mobilities Exceeding $107 \text{ cm}^2/\text{V s}$ in Modulation-Doped GaAs. *Appl. Phys. Lett.* **1989**, *55*, 1888.
- (51) Bechtel, H. A.; Muller, E. A.; Olmon, R. L.; Martin, M. C.; Raschke, M. B. Ultrabroadband Infrared Nanospectroscopic Imaging. *Proc. Natl. Acad. Sci. U. S. A.* **2014**, *111*, 7191–7196.
- (52) Johns, R. W.; Bechtel, H. A.; Rønnerstrom, E. L.; Agrawal, A.; Lounis, S. D.; Milliron, D. J. Direct Observation of Narrow Mid-Infrared Plasmon Linewidths of Single Metal Oxide Nanocrystals. *Nat. Commun.* In Press. DOI: [10.1038/ncomms11583](https://doi.org/10.1038/ncomms11583).
- (53) Huth, F.; Govyadinov, A.; Amarie, S.; Nuansing, W.; Keilmann, F.; Hillenbrand, R. Nano-Ftir Absorption Spectroscopy of Molecular Fingerprints at 20 nm Spatial Resolution. *Nano Lett.* **2012**, *12*, 3973–3978.
- (54) Abb, M.; Wang, Y.; Papasimakis, N.; de Groot, C. H.; Muskens, O. L. Surface-Enhanced Infrared Spectroscopy Using Metal Oxide Plasmonic Antenna Arrays. *Nano Lett.* **2014**, *14*, 346–352.
- (55) Rodrigo, D.; Limaj, O.; Janner, D.; Etezadi, D.; García de Abajo, F. J.; Pruneri, V.; Altug, H. Mid-Infrared Plasmonic Biosensing with Graphene. *Science* **2015**, *349*, 165–168.
- (56) Boyuk, D. S.; Chou, L.-W.; Filler, M. A. Strong Near-Field Coupling of Plasmonic Resonators Embedded in Si Nanowires. *ACS Photonics* **2016**, *3*, 184–189.
- (57) Adato, R.; Yanik, A. A.; Amsden, J. J.; Kaplan, D. L.; Omenetto, F. G.; Hong, M. K.; Erramilli, S.; Altug, H. Ultra-Sensitive Vibrational Spectroscopy of Protein Monolayers with Plasmonic Nanoantenna Arrays. *Proc. Natl. Acad. Sci. U. S. A.* **2009**, *106*, 19227–19232.
- (58) Tao, A.; Sinsermsuksakul, P.; Yang, P. Tunable Plasmonic Lattices of Silver Nanocrystals. *Nat. Nanotechnol.* **2007**, *2*, 435–440.
- (59) Dong, A.; Chen, J.; Vora, P. M.; Kikkawa, J. M.; Murray, C. B. Binary Nanocrystal Superlattice Membranes Self-Assembled at the Liquid-Air Interface. *Nature* **2010**, *466*, 474–477.
- (60) Nie, Z.; Petukhova, A.; Kumacheva, E. Properties and Emerging Applications of Self-Assembled Structures Made From Inorganic Nanoparticles. *Nat. Nanotechnol.* **2010**, *5*, 15–25.
- (61) Chen, H.-Y.; Lin, M.-H.; Wang, C.-Y.; Chang, Y.-M.; Gwo, S. Large-Scale Hot Spot Engineering for Quantitative SERS at the Single-Molecule Scale. *J. Am. Chem. Soc.* **2015**, *137*, 13698–13705.
- (62) Park, J.; An, K.; Hwang, Y.; Park, J.-G.; Noh, H.-J.; Kim, J.-Y.; Park, J.-H.; Hwang, N.-M.; Hyeon, T. Ultra-Large-Scale Syntheses of Monodisperse Nanocrystals. *Nat. Mater.* **2004**, *3*, 891–895.
- (63) Hautier, G.; Miglio, A.; Ceder, G.; Rignanese, G.-M.; Gonze, X. Identification and Design Principles of Low Hole Effective Mass P-Type Transparent Conducting Oxides. *Nat. Commun.* **2013**, *4*, 2292.
- (64) Hautier, G.; Miglio, A.; Waroquiers, D.; Rignanese, G.-M.; Gonze, X. How Does Chemistry Influence Electron Effective Mass in Oxides? A High-Throughput Computational Analysis. *Chem. Mater.* **2014**, *26*, 5447–5458.
- (65) Zhang, L.; Zhou, Y.; Guo, L.; Zhao, W.; Barnes, A.; Zhang, H.-T.; Eaton, C.; Zheng, Y.; Brahlek, M.; Haneef, H. F.; et al. Correlated Metals as Transparent Conductors. *Nat. Mater.* **2016**, *15*, 204–210.